Accepted for publication in:

Angle-dependent light scattering in tissue phantoms for the case of thin bone layers with predominant forward scattering

Tom Witke[1], Eduard Kuhn[2], Fabian Teichert[1], Christian Goßler[3], Ulrich Theodor Schwarz[1], Angela Thränhardt[1]

[1] Institute of Physics, Technische Universität Chemnitz, 09107 Chemnitz, Germany
[2] Weierstraß Institute, Mohrenstraße 39, 10117 Berlin, Germany
[3] OptoGenTech GmbH, Friedrichstr. 3/4 37073 Göttingen, Germany

E-mail address: tom.witke@physik.tu-chemnitz.de

Abstract: The cochlea forms a key element of the human auditory system in the temporal bone. Damage to the cochlea continues to produce significant impairment for sensory reception of environmental stimuli. To improve this impairment, the optical cochlear implant forms a new research approach. A prerequisite for this method is to understand how light propagation, as well as scattering, reflection and absorption, takes place within the cochlea. We offer a method to study the light distribution in the human cochlea through phantom materials and Monte-Carlo simulations. The calculation of an angular distribution after scattering requires a phase function. Often approximate functions like Henyey-Greenstein, two-term Henyey-Greenstein or Legendre polynomial decompositions are used as phase function. An alternative is to exactly calculate a Mie distribution for each scattering event. This method provides a better fit to the data measured in this work.

Keywords: Mie scattering; light scattering; Monte Carlo; tissue simulating phantoms

1 Introduction

Those affected by sensorineural hearing loss can have some of their hearing restored with the help of an electrical cochlear implant (eCI) [1–3]. This involves transmitting acoustic environmental stimuli to the brain by means of electrical stimulation of the spiral ganglion neurons (SGNs). However electrical cochlear implants are limited in their function by a wide current spread resulting in a low resolution of the spectral coding of auditory information [3, 4]. A new method to avoid this limitation is an optical cochlear implant (oCI) [2,5,6]. Here, instead of electrodes, light emitters are placed along the tonotopic axis of the cochlea to stimulate the SGNs, which were made light sensitive through Optogenetics [7]. Light promises to have a higher spatial resolution than electrical excitation, thus increasing the spectral selectivity of artificial sound encoding [8, 9]. If this concept proves to be feasible in clinical applications, it could facilitate speech recognition in background noise as well as the understanding of music and melodies [2, 10]. For further development of the oCIs and to demonstrate the higher spatial resolution of light, we need to understand how light is scattered in the human cochlea. Considering the size and accessibility of the auditory system, the use of tissue-simulating objects to mimic the properties of human tissues can help to understand scattering and absorption behaviour of the human cochlea tissue [11–17]. These so-called "phantoms" have to be tuned, to match the desired tissue properties, and can then be used for a number of applications like initially testing system designs or comparing performance between systems [18]. For our research we want a phantom that mimics the optical properties within the human cochlea and is suitable for experimental and simulative investigation [18–20]. In the following, we will discuss a Monte-Carlo approach to simulate the spread of light of micro emitters through tissue phantoms and contrast it with an experimental method to understand the propagation of light through thin bone layers. These phantoms consist of a filler matrix and a proportion of homogeneous, spherical, polymer scatterers. For our simulative approach we combine a wave optical method, to calculate the Mie-scattering [21,22] behaviour on a single polymer sphere, with the ray optical approach of the Monte-Carlo simulation [23, 24]. In this way, we calculate the angle distribution of one scatterer which we utilize as the phase function for scattering events in the Monte-Carlo simulation. The phase function describes the spatial distribution of scattered light for a single scattering event. In both approaches we used a red-light source which resembles the actual emitters that are used in oCIs. Sources of that wavelength range have the advantage of better neural stimulation with less tissue scattering and a lower risk of phototoxicity [4]. Calculating the exact angle distribution for each scattering event has proven to yield a higher agreement with measurements of phantoms than a simulation of those layers by using the Henyey-Greenstein formula as approximated phase function.

2 Theory

2.1 Tissue phantoms

To create a phantom that behaves close to actual tissue when exposed to radiation, it is important to know the main optical characteristics of the tissue that interacts with light [18]. For that we want to match the scattering coefficient $\mu_s(\lambda)$, the absorption coefficient $\mu_a(\lambda)$ and the anisotropy factor $g(\lambda)$ (see Section 2.3) [18], which represents the intensity-weighted mean value of the cosine of the scattering angle θ and indicates the

directionality of the scattering. Considering the fact that the shape of the phase function is usually not known, the angle scattering distribution is often characterized by this single parameter, the anisotropy factor g [11, 17]. Since light within the cochlea will interact mainly with the bone tissue of this structure, it is important to find a phantom that approximates the corresponding scattering characteristics. For this purpose, it has proven successful to regard the bone of the cochlea as a layer of spherical, homogeneous scatterers. The known optical parameters of bone are listed in Table 1. Polymer spheres [25], which are placed in an epoxy [26] matrix with a packing fraction η, are used as phantom material to mimic the optical properties of bone according to the parameters of Table 1. The optical parameters of those polymer scatterers are calculated as described in Section 2.2 and are listed in Table 2. As an idealization, we neglect the absorption in the phantoms ($\mu_\mathrm{a}(\lambda) = 0$) (see Table 2). In Figure 1 we simulated a bone layer in intercellular fluid and the resulting scattering angle distribution with the optical parameters for μ_a and μ_s of Pifferi et al. [15] and a second simulation with a idealized $\mu_\mathrm{a} = 0.0\,\mathrm{cm}^{-1}$. One can see, that such small absorption coefficients have almost no impact on the scattering behaviour, so the absorption is neglectable her. The handling of the anisotropy factor

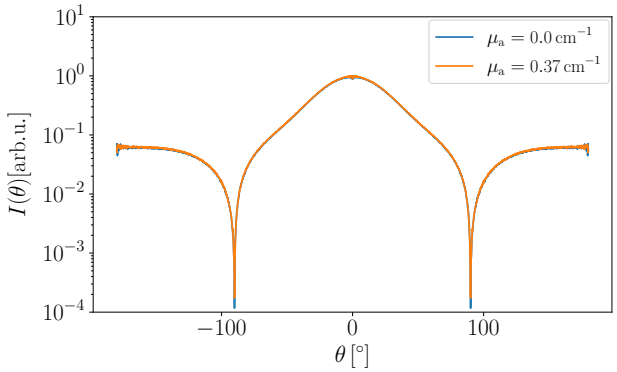

Figure 1: Simulated scattering angle distribution of a 100 µm bone layer for a wave, unpolarised to the plane of measurement with the known parameters of Pifferi et al. [15] (orange cuve) and with an idealized $\mu_\mathrm{a} = 0.0\,\mathrm{cm}^{-1}$ (blue curve).

g is explained in Section 2.3. By adjusting the packing fraction it is possible to fit the scattering properties (μ_s) for phantoms (Table 2) to the values of bone shown in Table 1. This is essential to calculate the scattering coefficient and the mean free path for the Monte Carlo simulation (see Section 2.2).

2.2 Scattering coefficient

Starting from the scattering efficiency of one polymer scatterer in epoxy, see the Appendix (Section 5.1), we calculate the effective cross section σ. Combined with a density of scatterers

$$\rho = \frac{\eta}{\frac{4}{3}\pi R^3} \tag{1}$$

with a volume packing fraction η and particle radius R, we calculate the scattering coefficient

$$\mu_\mathrm{s} = \sigma\rho \tag{2}$$

and the mean free path between two scattering events

$$l_\mathrm{s} = \frac{1}{\mu_\mathrm{s}} = \frac{1}{\rho\sigma} = \frac{4\pi R^3}{3\sigma\eta}. \tag{3}$$

Together with the angle dependent intensity distribution of unpolarised light for one scatterer (see Section 5.1), which is used as the phase function for the Monte-Carlo simulation

$$S_\mathrm{U}(\theta) = \frac{1}{2}(S_\perp + S_\parallel), \tag{4}$$

we can define a tissue layer with μ_s, l_s and with no need for an anisotropy factor g, since the shape of the phase function is defined through $S_\mathrm{U}(\theta)$. Alternatively, as a phase function, the Henyey-Greenstein function is often used as an approximation for the shape of an actual phase function for the scattering of radiation by a particle.

2.3 Henyey-Greenstein function

In the case of using the Henyey-Greenstein function, the anisotropy factor g can be calculated exactly from the intensity distribution $S_\mathrm{U}(\theta)$ for a single scattering event

$$g = \frac{\int_0^\pi S_\mathrm{U}(\theta)\sin\theta\cos\theta\,\mathrm{d}\theta}{\int_0^\pi S_\mathrm{U}(\theta)\sin\theta\,\mathrm{d}\theta}. \tag{5}$$

A g-value of $g = 1$ equals total forward scattering, $g = 0$ means isotropic scattering and $g = -1$ total backward scattering. We describe scattering of a single, homogeneous sphere with the angle dependent intensity distribution

$$p(\theta) = \frac{1}{4\pi}\frac{1-g^2}{(1+g^2-2g\cos\theta)^{\frac{3}{2}}}. \tag{6}$$

This gives us, together with the previously explained Mie distribution, see Appendix (Section 5.1), two possible phase functions to define a scattering event in the Monte-Carlo simulation. The first one uses the Mie distribution of light scattering on one sphere, i.e. equation (4). The later uses the Henyey-Greenstein function (6) with the addition of the anisotropy factor g calculated with (4) and (5).

2.4 Monte-Carlo simulation

To describe a layer of tissue with multiple scattering events, we can combine the previously introduced wave-optical description for a single scattering event with a Monte-Carlo simulation. These simulations for the light propagation require a free path length of the photons, scattering angles, as well as reflection or transmission at

Reference	λ in nm	$\mu_a(\lambda)$ in cm^{-1}	g	$\mu_s'(\lambda)$ in cm^{-1}	$\mu_s(\lambda)$ in cm^{-1}
Bashkatov et al. (2006) [12]	800	0.11	0.9	19.5	195
Pifferi et al. (2004) [15]	650	0.11		15.9	
Tauber et al. (2000) [16]	635	0.37	0.8	55.7	278.5
Firbank et al. (1993) [13]	650	0.4	0.93	26.2	374.28

Table 1: Known values of optical parameters of bone at different wavelengths λ with $\mu_s'(\lambda) = \mu_s(1-g)$.

Material	diameter in µm	refractive index m	μ_a in cm^{-1}	g	η	μ_s in cm^{-1}
Polymer [25]	1	1.587	0	0.95	0.00625	20.67
					0.0625	200.76
					0.01015	33.57
Epoxy [26]	-	1.519	-	-	$1-\eta$	-

Table 2: Values of optical parameters of polymer spheres at a wavelength of $\lambda = 635$nm and a packing fraction η in epoxy.

the boundaries of the layer. The probability that, in the Monte-Carlo simulation, a photon is scattered within a distance smaller than s is expressed by the probability distribution function $P(S < s)$. S is a random variable representing the distance that a photon travels between two scattering events. s is a value in the definition range of S, which is greater than zero [27].

$$P(S < s) = 1 - e^{-\mu_s s} \tag{7}$$

$P(s)$ is the probability distribution function. In contrast $f(s)$ is the probability density function, which expresses the probability that a photon is scattered while travelling between s and $s+ds$. The integral of each density function $f(s)$ is equal to the probability distribution function $P(s)$ [27],

$$P(s) = \int_{-\infty}^{s} f(s')\mathrm{d}s'. \tag{8}$$

A random number $a \in [0,1]$ with $a = P(s)$ is assigned to a random variable s, such as the path length of a photon. Equation (8) is used to obtain a series of values for a, which specify a series of values s. The histogram of the s-values corresponds to the probability density function $f(s)$. For the described problem, a steady-state simulation will be used. The aim is to find the intensity distribution after scattering processes.

To define a tissue layer in the Monte-Carlo simulation with the Mie distribution as phase function (equation 4), we first simulate a scattering event of an incoming plane wave on one polymer sphere in epoxy. In Figure 2 we show the angle distribution $p(\theta)$ for scattering events on different sized spheres, ranging from 50 nm to 3000 nm in diameter. With increasing size of the scatterers, the polarisation of the source becomes less important. Furthermore we see strong backward scattering for small spheres (50 nm, 100 nm) and increasing forward scattering with increased sphere size. Since we want to mimic the scattering behaviour in bone tissue, we aim for a diameter of the scatteres of 1000 nm. With this diameter the scattering distribution shows the Mie scattering regime and does not change when we look at different polarisations (see Figure 2). Therefore a scattering event in the Monte-Carlo simulation will result in an angle distribution which corresponds to the distribution on a single sphere with $d = 1000$ nm as shown in Figure 2. This distribution is calculated with Equation (4) which results out of the Equations (19) (see Section 5.1). The second step is to define a layer containing scatterers with radius r and calculating the packing fraction dependent mean free path between two scattering events and the scattering coefficient (see Section 2.2). Thus, the layer is defined with those parameters for the scatterer with the radius R. If we use Henyey-Greenstein as a phase function, the Monte-Carlo simulation additionally uses the computed anisotropy parameter g for a scattering event. In Figure 3 we can see how the mean free path depends on the size of the scatterers. Considering the density, l_s is propotional to $\frac{1}{R}$ in the range of Rayleigh scattering. In this range the scattering efficiency will decrease and l_s will increase for small radii compared to the wavelength ($R \ll \lambda$), because the cross section of the Rayleigh scattering is

$$\sigma(\omega) \approx \sigma_{Th} \frac{\omega^4}{\omega_0^4}, \tag{9}$$

with σ_{Th} as the Thomson effective cross section. As the radius increase, the scattering efficiency and μ_s increases, which in turn reduces the mean free path length due to $l_s = \frac{1}{\mu_s}$. Since the human cochlea consists of very thin bone layers, we aim to generate a strong forward scattering via small particles (see Table 2) and thin layers of polymer and epoxy mixtures. This will result in very few scattering events per photon which will contribute to the expected strong forward scattering of thin bone layers. We therefore use spheres which have the same order of magnitude in diameter as the used wavelength of the light source. The light source for each simulation run is defined as a beam consisting of 10^7 photons with a wavelength of $\lambda = 635$ nm. The layer thickness is varied between 100 µm and 500 µm. Like previously mentioned,

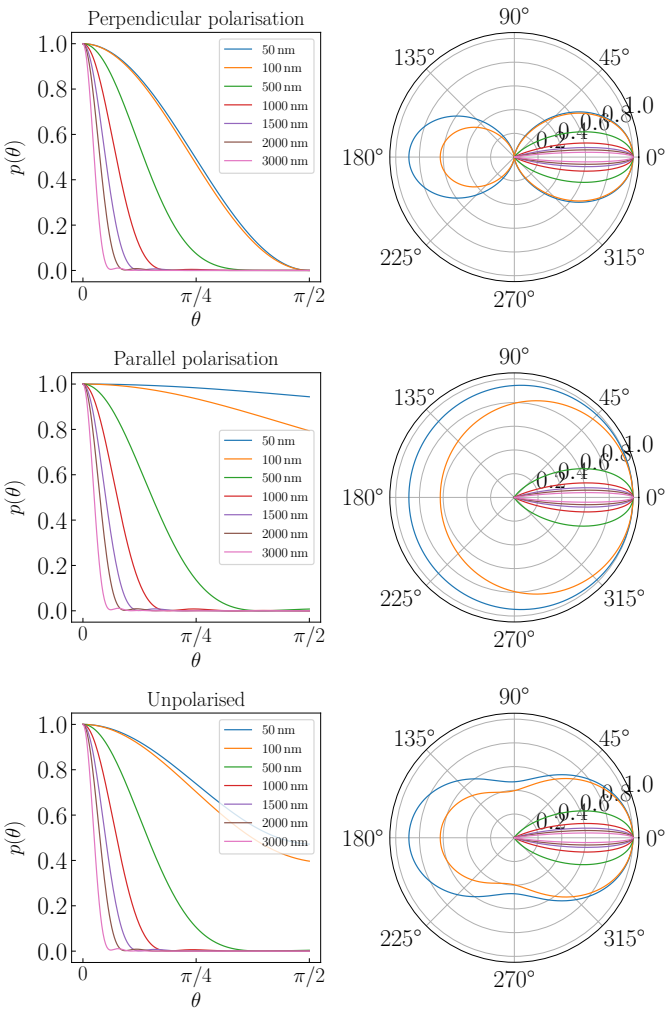

Figure 2: Scattering angle distribution on polymer spheres with a diameter between 50 nm and 3000 nm for a wave ($\lambda = 635\,\text{nm}$), perpendicular, parallel and unpolarised to the plane of measurment.

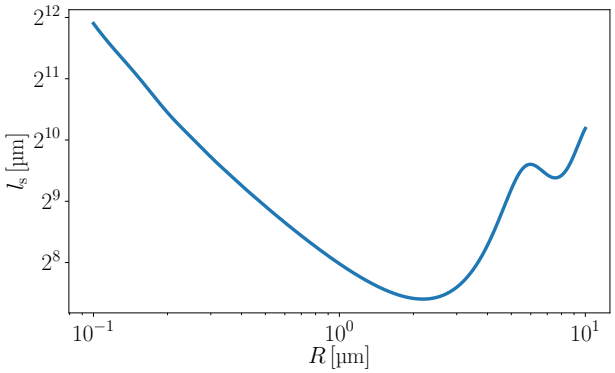

Figure 3: Double logarithmic plotted mean free path of photons versus radius R of the polymer spheres in the simulated layer for $\eta = 0.00625$ and $\lambda = 635\,\text{nm}$.

the spheres are placed in the medium with a packing fraction η. We will use $\eta = 0.00625$ and $\eta = 0.01015$ for a low number of scattering events. With those packing fractions we calculate the values for μ_s and g shown in Table 2.

The location and angle of every photon is saved when it reaches a border of the simulation box. This results in an angle distribution $p(\theta)$ which corresponds to the scattering intensity $I(\theta)$ with the scattering angle θ of the photon beam through the layer. To be able to make comparisons to measurements we normalized the angle distribution to the maximum of the values of the distribution.

2.5 Experimental approach

For sample preparation, the polymer spheres were mixed with a packing fraction of $\eta = 0.00625$ or $\eta = 0.01015$ with the epoxy medium for five minutes and then applied to the first glass plate with $m = 1.515$, $x_1 = 18\,\text{mm}$ (see Figure 4). The mixture was then hardened in vacuum for six hours. After that, the second glass plate was placed on the sample followed by completely drying the sample in vacuum. This procedure prevented the formation of air bubbles during both mixing and placement of the glass plates. The layer thickness of those samples is controlled via spacers which are manufactured according to the DIN 988 [28] standard and is, like in the simulation, varied between 100 µm and 500 µm. A schematic structure of a sample is shown in Figure 5.

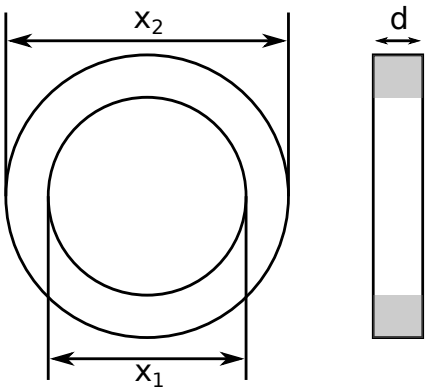

Figure 4: Dimensions of borosilicate glass and spacers for phantom samples with $x_1 = 18\,\text{mm}$, $x_2 = 25\,\text{mm}$ and $d = 0.1\,\text{mm}$, $d = 0.2\,\text{mm}$, $d = 0.3\,\text{mm}$ or $d = 0.5\,\text{mm}$.

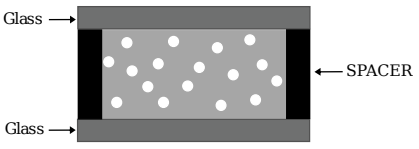

Figure 5: Schematic structure of a sample.

The experimental setup shown in figure 6, containing the described samples, the laser diode CPS635S [29] which has a wavelength of 635 nm, an elliptical, collimated output beam and the light sensors TSL2591 [30] and VEML7700 [31]. The sensors were mounted on an arm which rotates around the sample in a range of 230°. Measurements of the scattering intensity $I(\theta)$ with the

scattering angle θ are done in 1° steps in air behind the layer. Since the Monte-Carlo simulation does not include

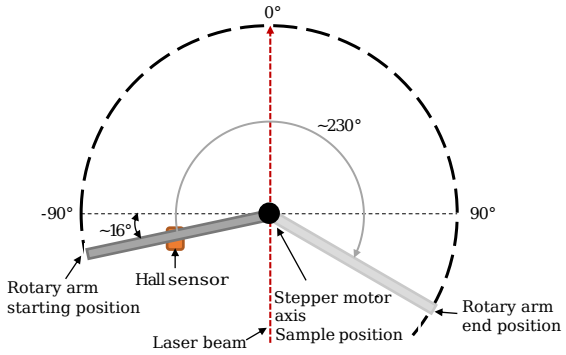

Figure 6: Schematic structure of the experimental setup.

any glass layers but is compared to our measurements we included a Snellius correction in the simulation,

$$\alpha = \arcsin\left(\frac{\sin\beta}{m_{\text{matrix}}}\right), \tag{10}$$

with α and β being the incoming and outgoing angle and m_{matrix} the refractive index of the surrounding epoxy medium. We can utilize the unpolarised transmission coefficient T_{u} as a threshold as a photon will get reflected with a predetermined probability. For that we generate a random number $z \in [0, 1]$. If z is smaller that T_{u} the coresponding photon will get transmitted. If not, the photon will get reflected. With this method, we can follow the reflection processes of each photon until it has actually left the layer. This compares favourably to a correction of the experimental data where we can only correct the first time a photon tries to exit the layer.

3 Comparison

As shown in Figure 7, we first modeled a scattering event on a single polymer scatterer. We use the calculations from section 5.1 wich are implemented in a Mie scattering module (PyMieScatt) [32]. The angle distribution shows the typical Mie scattering behaviour with a large amount of forward scattering, which is ideal for a layer of spheric scatterers. Therefore, the angle distribution is used as a phase function to define a scattering event in the Monte-Carlo simulation. Together with the scattering coefficient $\mu_{\text{s}} = 33.57\,\text{cm}^{-1}$, the packing-fraction-dependent mean free path $l_{\text{s}} = 297.80\,\mu\text{m}$, we obtain the angle distribution for $\eta = 0.01015$ and $d = 500\,\mu\text{m}$ shown in Figure 8 (orange curve). For these parameters, an average of 3.51 scattering events occur and 18.5 % of the photons remain unscattered. Compared to the scattering intensity of a single sphere, this results in a wider distribution, which is still mainly forward scattered. For the comparison in Figure 8 we excluded unscattered photons which make up a significant portion of the angle distribution. The blue curve in Figure 8 is the same distribution as shown in Figure 7 and the small blue

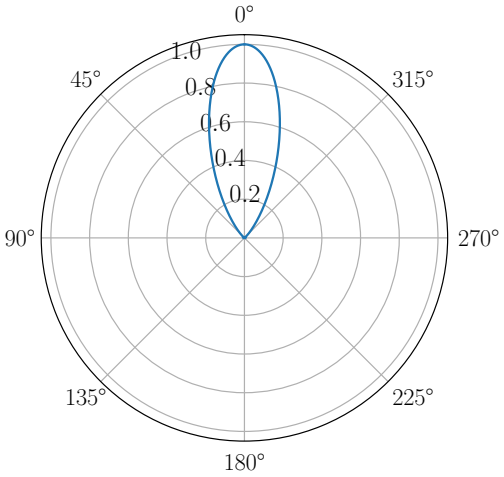

Figure 7: Scattering intensity $I(\theta)$ for one polymer sphere in epoxy resulting from a incoming wave wich is unpolarised to the direction of propagation.

curve is the backscattered light from said distribution. The same layer simulated with Henyey-Greenstein as phase function (see Figure 9 and Equation (6)) and an additional anisotropy factor of $g = 0.95$ (brown curve in Figure 9) results in the green curve. This distribution shows a more peaked pattern with less backscattering. If we compare theory and experiment, we see the angle

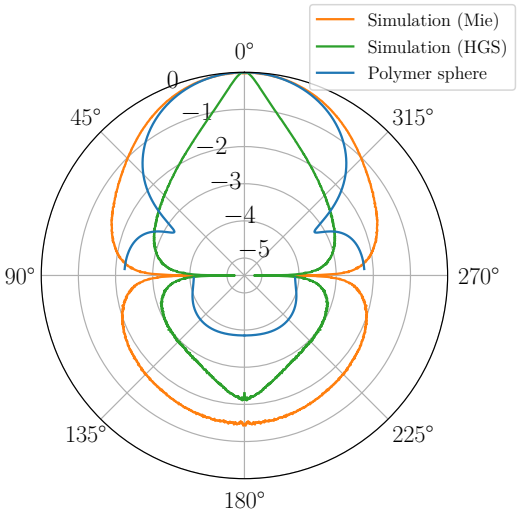

Figure 8: Logarithmically plotted scattering intensity $I(\theta)$ with Mie scattering as phase function (orange curve) and with Henyey-Greenstein as phase function (green curve) of a simulated $d = 500\,\mu\text{m}$ polymer-epoxy layer and for one polymer sphere in epoxy (blue curve).

distributions shown in Figure 11. Since the polarization of the incident light has no influence on the angular distribution in the prevailing size ratio of wavelength and sphere diameter, the unpolarized portion of the light is compared. In the measurements the unscattered light is included showing in a sharp distribution for small angles.

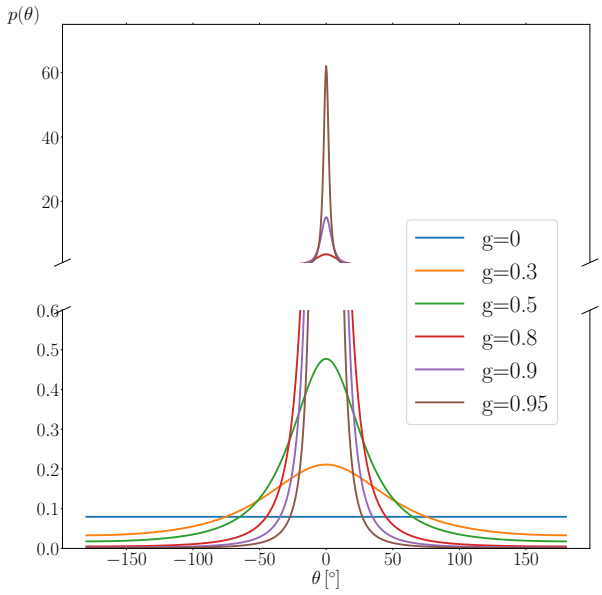

Figure 9: Henyey-Greenstein function for multiple g-values.

The Monte-Carlo simulation that uses the Mie distribution from one sphere as scattering function (blue curve) shows a strong agreement with the experimental data (green curve) for larger angles. The second Monte-Carlo simulation wich uses the Henyey-Greenstein function as scattering function (orange curve) produces lower values than the measured data. All three approaches show a strong forward directed scattering behaviour with a large proportion of unscattered light (compare Figure 8). Since we broadened the unscattered light of the simulations with a Gaussian fit to a zero measurement of the laser through an epoxy layer (see Figure 10), comparisons of the curve form between simulations and measurements in the range of $0 - 14°$ are not meaningful. Nevertheless, the proportion of unscattered light can be detected and compared in this area. The discrepancy between the simulation methods at small angles decreases with reducing the layer thickness. In Figure 12 we consider a thinner

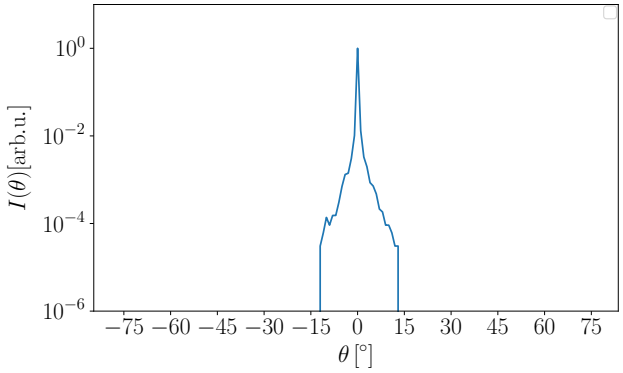

Figure 10: Logarithmically plotted measured scattering intensity of a $d = 100\,\mu\text{m}$ epoxy layer.

layer, which is $d = 200\,\mu\text{m}$ thick with a packing fraction of $\eta = 0.01015$, $\mu_s = 33.57\,\text{cm}^{-1}$ and $l_s = 297,80\,\mu\text{m}$. Here, the agreement between both simulation methods is very high for small angles. For larger angles, the Monte Carlo simulation with the Mie distribution also has a higher agreement with the experimental data for this thinner layer than with the Henyey-Greenstein function. For layers with few scattering events simulations with an exactly calculated distribution as phase function seem to better represent experimental data for large angles than simulations that use the Henyey-Greenstein as phase function.

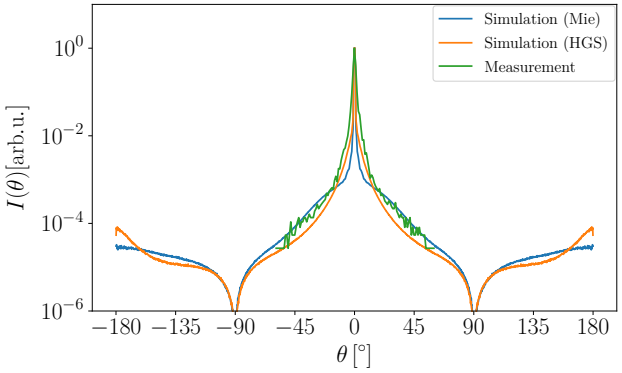

Figure 11: Logarithmically plotted measued scattering intensity (green curve) of a $d = 500\,\mu\text{m}$ polymer-epoxy layer compared to the Monte-Carlo simulation with Mie distribution (blue curve) and the Monte-Carlo simulation with HGS for the corresponding parameter set.

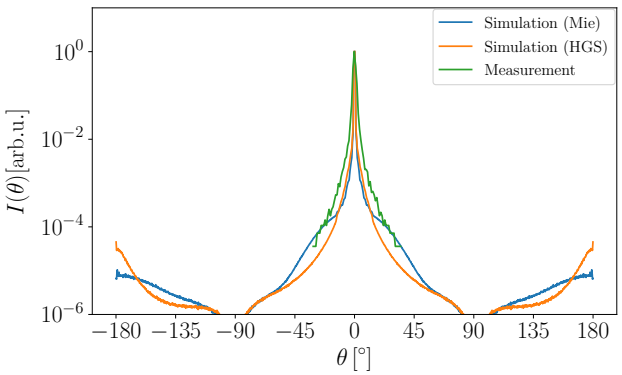

Figure 12: Logarithmically plotted measued scattering intensity (green curve) of a $d = 200\,\mu\text{m}$ polymer-epoxy layer compared to the Monte-Carlo simulation with Mie distribution (blue curve) and the Monte-Carlo simulation with HGS for the corresponding parameter set.

4 Summary and conclusions

We investigated the scattering properties of human tissue by using polymer-epoxy layers as phantoms. On the one hand, this was done with a Monte-Carlo simulation with which we showed that for a description of scattering

in tissue, the Henyey-Greenstein function is not necessary, but the scattering distribution of a scatterer as a phase function provides an accurate description of the behaviour of light in a tissue layer. Together with the mean free path l_s and its corresponding scattering coefficient μ_s, which are calculated from one scattering event, we are able to define tissue layers without using the Henyey-Greenstein, or another approximated phase function. This is supported by an experimental investigation in which the agreement between the simulative method and the corresponding measurements of the simulated layers is shown. For layers with few scattering events, the Mie distribution as phase functions shows higher agreement with the experimental data than the Henyey-Greenstein function for large angles. Therefore calculating the exact phase function for every scattering event has proven to provide a more realistic scattering behaviour in tissue layers than the often used Henyey-Greenstein function wich is one of any function that meets the condition of normalization

$$2\pi \int_0^\pi p(\theta) \sin\theta \, \mathrm{d}\theta = 1 \tag{11}$$

and anisotropy

$$2\pi \int_0^\pi p(\theta) \cos\theta \sin\theta \, \mathrm{d}\theta = g. \tag{12}$$

To find an analytic phase function that is more consistent with the exact Mie distribution, one could search for a function that fits the Mie angle distribution and therefore meets the said conditions. This has the advantage that the phase function is not just an assumption but is based on a calculated distribution. In further work we will provide this kind of function together with an analytical model, thereby calculating the angle distributions and transmissions after any number of scattering events. To improve the presented approach and make it come closer to real tissue one should consider multiple sphere sizes in the layers. For this purpose, we will produce appropriate phantoms in subsequent work and perform corresponding measurements and simulations. In addition, we will investigate the scalability of phantom layers to create structures that have the shape and optical properties of a human cochlea. This will allow further investigation of the scattering behaviour of an emitter array in the human cochlea.

5 Appendix

5.1 Mie scattering theory

The interaction of an electromagnetic wave with spherical, homogeneous scatterers is the subject of Lorenz-Mie theory [33]. If one considers a spherical scatterer in isolation, taking this theory into account, scattering parameters for a single scattering event within a layer can be calculated on this sphere. The incident light can be described as a plane wave polarized in the x-direction

$$\vec{E}_\mathrm{in} = \vec{E}_0^{i\vec{k}\cdot\vec{r}}\vec{e}_x = E_0 e^{ikr\cos\theta}\vec{e}_x \tag{13}$$

which gets scattered into a wave

$$\vec{E}_\mathrm{s} = \sum_{n=1}^{\infty} E_\mathrm{n}(i a_\mathrm{n}\vec{N}^{(3)}_{\mathrm{e1n}}(k,\vec{r}) - b_\mathrm{n}\vec{M}^{(3)}_{\mathrm{o1n}}(k,\vec{r})). \tag{14}$$

The scattered wave is composed of real and imaginary parts which in turn consist of vectorial, spherical harmonics which result out of the known Maxwell equations. $\vec{N}$ and $\vec{M}$, which depend on the wave vector k and the radial component $\vec{r}$, contain the spherical Hankel functions of the first kind (superscript (3)). The indices e and o mean even/odd (symmetrical/antisymmetrical). The scattered waves overlap with the part of the plane wave that remains unscattered. The coefficients

$$a_\mathrm{n} = \frac{\psi_\mathrm{n}(z)\psi_\mathrm{n}'(mz) - m\psi_\mathrm{n}(mz)\psi_\mathrm{n}'(z)}{\zeta_\mathrm{n}(z)\psi_\mathrm{n}'(mz) - m\psi_\mathrm{n}(mz)\zeta_\mathrm{n}'(z)} \tag{15}$$

$$b_\mathrm{n} = \frac{m\psi_\mathrm{n}(z)\psi_\mathrm{n}'(mz) - \psi_\mathrm{n}(mz)\psi_\mathrm{n}'(z)}{m\zeta_\mathrm{n}(z)\psi_\mathrm{n}'(mz) - \psi_\mathrm{n}(mz)\zeta_\mathrm{n}'(z)} \tag{16}$$

are the amplitudes of the partial waves that make up the scattered wave [33]. They consist of the Ricatti-Bessel functions $\zeta(x)$ and $\psi(x)$ which depend on the ratio of particle circumference to wavelength

$$z = \frac{\pi d}{\lambda} \tag{17}$$

as well as the complex refractive index

$$m = m_\mathrm{r} - i m_\mathrm{i} \tag{18}$$

and are derived from the Hankel-Bessel functions. From the coefficients a_n, b_n we calculate the polarization-dependent scattering intensities

$$S_1 = \sum_{n=1}^{n_\mathrm{max}} \frac{2n+1}{n(n+1)}(a_n\pi_n + b_n\tau_n) \tag{19}$$

$$S_2 = \sum_{n=1}^{n_\mathrm{max}} \frac{2n+1}{n(n+1)}(a_n\tau_n + b_n\pi_n) \tag{20}$$

$$S_\perp(\theta) = |S_1|^2 \tag{21}$$

$$S_\parallel(\theta) = |S_2|^2 \tag{22}$$

$$S_\mathrm{U}(\theta) = \frac{1}{2}(S_\perp + S_\parallel) \tag{23}$$

and the scattering efficiency

$$Q_\mathrm{sca} = \frac{2}{z^2}\sum_{n=1}^{\infty}(2n+1)\{|a_n|^2 + |b_n|^2\}. \tag{24}$$

U stands for "unpolarised". The factors π and τ are calculated as follows

$$\pi_n = \frac{2n-1}{n-1}\cos(\theta)\pi_{n-1} - \frac{n}{n-1}\pi_{n-2} \tag{25}$$

$$\tau_n = n\cos(\theta)\pi_n - (n+1)\pi_{n-1} \tag{26}$$

with $\pi_1 = 1$, $\pi_2 = 3\cos\theta$ and $\tau_1 = \cos\theta$, $\tau_2 = 3\cos(2\cos^{-1}(\cos\theta))$.

6 Author Contributions

Tom Witke was involved in writing the manuscript, realising the simulation and measurments. Eduard Kuhn and Fabian Teichert made contriubtions in implementations of the simulation and experiment. Christian Goßler contributed to the experimental setup and manufacturing the tissue phantoms. Ulrich Schwarz and Angela Thränhardt gave advice on the structure and implementation and replied to emerging questions as necessary. All authors contributed to reviewing the manuscript. Tom Witke is the corresponding author of this paper.

7 Conflict of Interest

The authors have no relevant financial interests in this articleand no potential conflicts of interest to disclose.

8 Data Availability Statement

The Data can be requested by contacting the corresponding author, Tom Witke. Prior consent from the subjects and necessary approvals from the authors institutional committees will be required to obtain the data.

References

[1] A. Huet, and V. Rankovic: Application of Targeting-Optimized Chronos for Stimulation of the Auditory Pathway 2020, Humana, New York.

[2] M. Jeschke, and T. Moser: Considering optogenetic stimulation for cochlear implants, Hearing Research 322 (2015), 224–234.

[3] F. Zeng, S. Rebscher, W. Harrison, X. Sun, and H. Feng: Cochlear implants: system design, integration, and evaluation, IEEE Reviews in Biomedical Engineering 1 (2008), 115–142.

[4] D. Keppeler, R. M. Merino, D. Lopez de la Morena, B. Bali, A. T. Huet, A. Gehrt, C. Wrobel, S. Subramanian, T. Dombrowski, F. Wolf, V. Rankovic, A. Neef, and T. Moser: Ultrafast optogenetic stimulation of the auditory pathway by targeting-optimized Chronos, The EMBO Journal 37 (2018), 1–11.

[5] V. H. Hernandez, A. Gehrt, K. Reuter, Z. Jing, M. Jeschke, A. M. Schulz, G. Hoch, M. Bartels, G. Vogt, C. W. Garnham, H. Yawo, Y. Fukazawa, G. J. Augustine, E. Bamberg, S. Kügler, T. Salditt, L. de Hoz, N. Strenzke, and T. Moser: Optogenetic stimulation of the auditory pathway, The Journal of Clinical Investigation 124 (2014), 1114–1129.

[6] D. Keppeler, C. Kampshoff, A. Thirumalai, C. Duque-Afonso, J. Schaeper, T. Quilitz, M. Töpperwien, C. Vogl, R. Hessler, A. Meyer, T. Salditt, and T. Moser: Multiscale photonic imaging of the native and implanted cochlea, PNAS 118 (2021), 1–11.

[7] C. Wrobel, A. Dieter, A. Huet, D. Keppeler, C. J. Duque-Afonso, C. Vogl, G. Hoch, M. Jeschke, and T. Moser: Optogenetic stimulation of cochlear neurons activates the auditory pathway and restores auditory-driven behavior in deaf adult gerbils, SCIENCE TRANSLATIONAL MEDICINE 10 (2018), 1–12.

[8] C. G. Tobias Moser, Daniel Keppeler, and U. T. Schwarz: Hearing the Light, OPTICS & PHOTONICS NEWS 32 (2021), 42–53.

[9] A. Dieter, D. Keppeler, and T. Moser: Towards the optical cochlear implant: optogenetic approaches for hearing restoration, EMBO Molecular Medicine 12 (2020), 1–16.

[10] G. Kohlberg, J. Spitzer, D. Mancuso, and A. Lalwani: Does Cochlear Implantation Restore Music Appreciation?, The Laryngoscope 124 (2014), 583–811.

[11] A. N. Bashkatov, E. A. Genina, V. I. Kochubey, and V. V. Tuchin: Optical properties of human skin, subcutaneous and mucous tissues in the wavelength range from 400 to 2000 nm, Journal of Physics D: Applied Physics 38 (2005), 2543–2555.

[12] A. Bashkatov, E. Genina, V. Kochubey, and V. Tuchin: Optical properties of human cranial bone in the spectral range from 800 to 2000 nm, Progress in Biomedical Optics and Imaging - Proceedings of SPIE 6163 (2006), 12.

[13] M. Firebank, M. Hiraoka, M. Essenpreis, and D. Delpy: Measurement of the optical properties of the skull in the wavelength range 650-950 nm, Physics in Medicine and Biology 38 (1993), 9.

[14] E. Genina, A. Bashkatov, and V. Tuchin: Optical Clearing of Cranial Bone, Advances in Optical Technologies 2008 (2008), 8.

[15] A. Pifferi, A. Torricelli, P. Taroni, A. Bassi, E. Chikoidze, E. Giambattistelli, and R. Cubeddu: Optical biopsy of bone tissue: a step toward the diagnosis of bone pathologies, Journal of Biomedical Optics 9 (2004), 7.

[16] S. Tauber, R. Baumgartner, K. Schorn, and W. Beyer: Lightdosimetric Quantitative Analysis of the Human-Petrous Bone: Experimental Study for Laser Irradiationof the Cochlea, Lasers in Surgery and Medicine 28 (2001), 9.

[17] W. Cheong, S. Prahl, and A. Welch: A Review of the Optical Properties of Biological Tissues, Journal of Quantum Eletronics 26 (1990), 2166–2185.

[18] B. W. Pogue, and M. S. Patterson: Review of tissue simulating phantoms for optical spectroscopy, imaging and dosimetry, Journal of Biomedical Optics 11 (2006), 1–16.

[19] S. Jacques, C. Alter, and S. Prahl: Angular Dependence of HeNe Laser Light Scattering by Human Dermis, Lasers in the Life Sciences 1 (1987), 309–333.

[20] S. Johannsmeier, J. Wenzel, M. L. Torres-Mapa, S. Junge, P. Sasse, J. D. Stockhausen, T. Ripken, D. Heinemann, and A. Heisterkamp: Light-cell interactions in depth-resolved optogenetics, Biomedical Optics Express 11 (2020), 6536–6550.

[21] W. Wiscombe: Mie Scattering Calculations: Advances in Technique and Fast, Vector-speed Computer Codes 1979, NASA, Washington, D.C., DC, United States.

[22] W. Wiscombe: Improved Mie Scattering Algorithms, Applied optics 19 (1980), 1505–1509.

[23] B. J. Sumlin, W. R. Heinson, and R. K. Chakrabarty: Retrieving the aerosol complex refractive index using PyMieScatt: A Mie computational package with visualization capabilities, Journal of Quantitative Spectroscopy and Radiative Transfer 205 (2018), 127–134.

[24] T. Yang, B. Glorieux, K. Shiau, Y. Chang, Y. Yu, and C. Sun: Improving light output by micro-TiO 2 scatters in pc-WLED encapsulants, Optics Express 30 (2022), 1–11.

[25] Polysciences Inc. Polybead Microspheres.

[26] Epoxy Technology. EPO-TEK 301, https://www.epotek.com/docs/en/Datasheet/301.pdf.
[27] T. Lister, P. A. Wright, and P. H. Chappell: Optical properties of human skin, Journal of Biomedical Optics 17 (2012), 1–15.
[28] Mädler GmbH. Passscheiben DIN 988, https://www.maedler.de/product/1643/1126/3445/passscheiben-din-988.
[29] Thorlabs, Inc. CPS635S, https://seltokphotonics.com/upload/iblock/e3b/e3b3ea987c473fcfe1e0746c1af210a1.pdf.
[30] Adafruit Industries. TSL2591, https://cdn-shop.adafruit.com/datasheets/TSL25911_Datasheet_EN_v1.pdf.
[31] Vishay Intertechnology, Inc. VEML7700, https://www.vishay.com/docs/84323/designingveml7700.pdf.
[32] PyMieScatt, https://pymiescatt.readthedocs.io/en/latest/.
[33] C. Bohren, and D. Huffman: Absorption and Scattering of Light by Small Particles 1998, WILEY-VCH Verlag GmbH & Co. KGaA, Weinheim, Germany.